NONLINEAR EVOLUTION OF KINK-UNSTABLE MAGNETIC FLUX TUBES AND SOLAR δ-SPOT ACTIVE REGIONS

M. G. LINTON,[1] R. B. DAHLBURG,[2] G. H. FISHER,[1] AND D. W. LONGCOPE[1,3]

ABSTRACT

The motivation for the work described in this paper is to understand kink-unstable magnetic flux tubes and their role in the formation of δ-spot active regions. It has been proposed that, during their rise to the photosphere, a certain fraction of convection zone flux tubes become twisted to the point where they are unstable to the current driven kink instability. These kink-unstable flux tubes then evolve toward a new, kinked equilibrium as they continue to rise to the photosphere, appearing as δ-spot groups upon emergence. Because of their kinked nature, these flux tubes could be highly susceptible to flaring, explaining the very active nature of δ-spot groups.

We study the kinking flux tube problem with a three-dimensional numerical model containing only the most basic features of a kink-unstable flux tube. We build on our earlier work describing the linear phase of the kink instability, and follow the evolution into the nonlinear regime: (1) We perform numerical simulations of constant-twist, kink-unstable flux tubes in an initially cylindrical equilibrium configuration in three dimensions, in a high-β pressure-confined environment. We consider many different initial configurations, including the Gold-Hoyle flux tube. (2) These numerical calculations confirm the growth-rate predictions of our earlier work, when viscous dissipation is included. They also confirm our velocity profile predictions. (3) The flux tubes evolve toward new helically symmetric equilibrium configurations. (4) The timescale for saturation to the kinked equilibrium configuration is $\tau_{\mathrm{sat}} \sim 10/\omega_0$, where ω_0 is the linear growth rate calculated as in the earlier paper. (5) The cylindrically symmetric part of the kinked equilibrium is well described by the $m = 0$ Chandrasekhar-Kendall functions (i.e., the Lundquist field). The $m = 1$ helically symmetric part, however, is not well described by the $m = 1$ Chandrasekhar-Kendall functions. (6) The equilibrium kink amplitudes are not large, at less than one-third of the tube radius. (7) The peak kinetic energy of the instability can be predicted from the initial excess perpendicular magnetic energy. (8) The amplitudes of the kinked tubes are large enough to give a δ-spot region tilt angle of up to 30° away from that of an unkinked tube.

Subject headings: MHD — Sun: activity — Sun: interior — Sun: magnetic fields — sunspots

1. INTRODUCTION

Solar active regions as observed in the photosphere are regions of strong magnetic field concentration (~ 2 kG, as compared to quiet-region average field strength of the order of a few gauss). Active regions generally consist of two adjacent areas of opposite magnetic polarity, which, when viewed in X-rays, are seen to be joined by coronal loops. This leads to the commonly held interpretation that active regions are the tops of magnetic flux loops which emerge from the convection zone through the photosphere and into the corona. The visible parts of these flux tubes (at the photosphere and above) are believed to be the apices of large Ω-shaped loops that have risen through the convection zone.

The source of these flux tubes is most likely the base of the convection zone where differential rotation is thought to generate azimuthal field from poloidal field (see, e.g., reviews by DeLuca & Gilman 1991; Hughes 1992). The base of the convection zone, or the convective overshoot region, in addition to being the location of field generation, is also believed to be the only stable place where magnetic flux can live for long periods of time.

Emerging flux tubes are created from this source of azimuthal field, and their subsequent buoyant rise has been studied, using numerical models employing the "thin flux tube" approximations (Choudhuri & Gilman 1987; Fan, Fisher, & DeLuca 1993; Moreno-Insertis, Caligari, & Schüssler 1994; Caligari, Moreno-Insertis, & Schüssler 1995). The success of these models at predicting and reproducing active region properties, such as latitude of emergence, relative motion of opposite polarities after emergence, and the angles by which the active regions are tilted away from the equator, lends credence to the paradigm that flux tubes rise through the entire convection zone before emerging through the photosphere.

These models, however, only explain the majority of the active regions that follow Hale's law (Zirin 1988, p. 307). These active regions consist of leading and following spots in a spot group aligned approximately parallel to the equator. Left unexplained are some of the more unusual active region configurations, in particular, "island δ-spots" (e.g., Zirin 1988, p. 337). These are active regions where the opposite polarity regions are very close to each other, almost touching, and the spot pairs are inclined at a significant angle to the equator. In contrast to normal active regions, where the spots separate as the region evolves, δ-spots tend to rotate and remain compact as they emerge. More than just being an anomaly unexplained by the present rising flux tube models, these regions are of interest because they are much more likely to flare than other active regions (see, e.g., Tanaka 1980).

[1] Space Sciences Laboratory, University of California, Berkeley, Berkeley, CA 94720.
[2] Laboratory for Computational Physics and Fluid Dynamics, Naval Research Laboratory, Washington, DC 20375-5344.
[3] Department of Physics, Montana State University, Bozeman, MT 59717.

In § 2 we discuss the evidence that these δ-spots are caused by flux tubes which, rather than having the usual planar Ω-loop structure, have been deformed into braided Ω-loops. We then present the evidence, based on the topological quantities twist and writhe, that the loops have been deformed by the current driven kink instability rather than by helical convection zone flows.

This evidence motivates us to study the evolution of rising, kink-unstable flux tubes in the convection zone. We would like to learn what characterizes the shape of a kinked flux tube after the instability has saturated (if it does indeed saturate), and what the timescale for this saturation is. In this paper we report on our investigation of a simplified version of this problem. We simulate the kink instability in an infinitely long, initially cylindrically symmetric flux tube in a high-β atmosphere without gravity. We expect to obtain general characteristics of the kink instability as relevant to the problem at hand from this study. While other effects, such as the curvature of a flux tube or the expansion of a tube as it rises through a gravitationally stratified atmosphere, may affect the behavior of a kinking flux tube, we leave those effects for future studies.

We discuss the linear theory of the kink instability in § 3, and give a brief summary of the predictions that our earlier linear analysis makes about the instability. In § 4 we discuss the three-dimensional numerical MHD code and the initial conditions we used to model the nonlinear evolution of the kink instability. In § 5 we discuss the results of the study. We compare the linear phase of the instability from the numerical simulations with the behavior predicted by our linear stability analysis, and then discuss the nonlinear behavior and characterize the saturation equilibrium. In § 6 we summarize the results and discuss their implications.

2. δ-SPOTS AS KINKED Ω-LOOPS

A likely explanation for the morphology and activity of δ-spot active regions is that they are caused by a braided or kinked tube rather than a simple Ω-loop. A braided structure would bring different sections of the tube quite close to each other, possibly even in contact with each other. This would explain the closeness of the regions in a δ-spot, as well as their propensity to flare, since magnetic reconnection could occur at the regions of contact. A braided structure would also explain the orientation and evolution of δ-spots. A simple Ω-loop flux tube will be a nearly planar object, parallel to the equator, and the footpoints which mark its intersection with the photosphere will also lie on a line nearly parallel to the equator. A kinked or braided Ω-loop, as we envision it, would also be basically parallel to the equator except for a critical section near the apex of the loop which has kinked, as shown in Figure 1. The line joining the footpoints of this kinked or braided loop could initially appear significantly tilted away from the equator, as shown in the inset marked T1. This inset shows the footpoints of the tube when the photosphere intersects the tube at the plane marked T1 in the main figure. This line would then rotate as the tube rose further, as shown in insets T2 and T3, again representing the corresponding planes in the main figure. Several researchers have followed the evolution and rotation of δ-spots and have found footpoint orientations and rotations similar to those shown in Figure 1, leading them to conclude that δ-spot evolution is well explained by the rising or sinking of braided structures (Tanaka 1991, Figs. 1 and 6; Kurokawa et al. 1994; Leka et
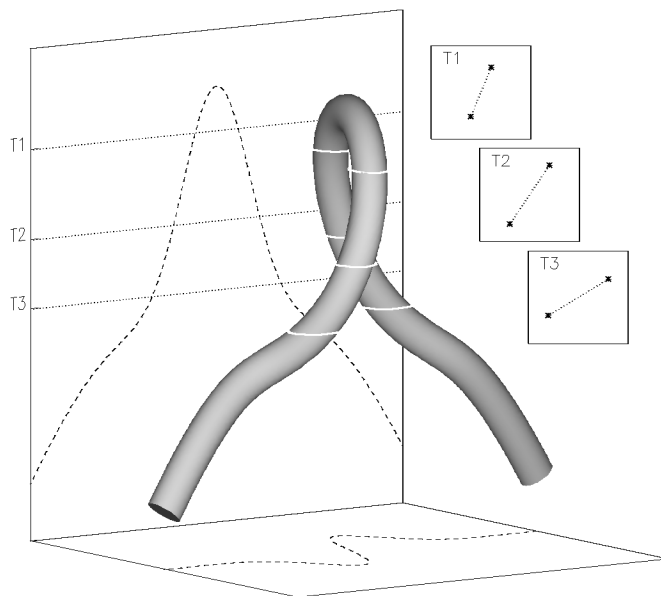

FIG. 1.—Schematic picture of a rising, kinked flux tube. The dotted horizontal lines represent the planes at which the tube intersects the photosphere at different times. These planes are plotted to the right of the main figure to illustrate how the tilt angle changes as the tube rises.

al. 1996, Fig. 3). In addition, Lites et al. (1995) and Leka et al. (1996) found the magnetic field of the δ-spots they observed to be highly twisted.

Proposed mechanisms for creating these braided Ω-loops involve either fluid motions of the convection zone (Gold & Hoyle 1960; Barnes & Sturrock 1972) or the current driven kink instability (Tanaka 1991). Fortunately, conservation of magnetic helicity leads to an observable difference between the two possibilities. The helicity of a flux tube can be written as the sum of two terms called the *writhe* and the *twist* (Berger & Field 1984; Moffatt & Ricca 1992). The writhe depends only on the configuration of the tube's axis, while the twist depends only on the structure of field lines within the tube. The sum of these two quantities (i.e., the total helicity) is conserved under ideal MHD motion, so an increase in writhe, for instance, must be accompanied by a decrease in twist. A straight tube (zero writhe) with initially left-handed twist in its magnetic field will be unstable to a kink that deforms its axis into a left-handed helix, turning (negative) twist into (negative) writhe while conserving helicity (Linton, Longcope, & Fisher 1996, hereafter LLF). On the other hand, an initially straight tube that is deformed by helical convective motions into a right-handed helix (adding positive writhe) will have a left-handed twist induced on its field lines (adding negative twist) to conserve the total helicity (Longcope & Klapper 1997). Thus a tube writhed by the kink mode will *always* have the same sign of writhe and twist, but the same is not true for a tube writhed by convection zone flows. In the latter case the final state will depend on the sign and magnitude of the initial twist compared to the writhe. If the induced twist is larger than the initial twist, the final state will have opposite signs of twist and writhe. If the initial twist is larger, then there will be little or no correlation between the final twist and writhe. Any correlation in this situation would be due to a slight preference for both twist and kinetic helicity to be negative (positive) in the northern (southern) hemisphere (e.g., Pevtsov & Canfield

1997; Longcope, Fisher, & Pevtsov 1998), but as this is only a slight preference superimposed on a large scatter, it would lead at most to a small correlation. Therefore one could test the cause of δ-spot writhe by observing the relative sign of writhe and twist for a large number of cases. If the vast majority had the same sign, the cause would clearly be the kink instability. On the other hand if there were only a weak preference, the cause could be attributed to convection zone motions. Leka et al. (1996) performed a study like this on a small scale, observing a few δ-spots, and found them to have the same sign of twist and writhe. While extending their study to a larger number of δ-spots is beyond the scope of this paper, it should be possible to carry out given presently available data.

3. THE LINEAR REGIME OF THE KINK INSTABILITY

When field lines of a flux tube are twisted sufficiently, the tube spontaneously deforms into a helical shape and thereby releases some of the magnetic energy stored in the tension of its twisted field lines. In other words, twist is replaced by writhe in such a way that the total magnetic energy is decreased while the helicity remains constant. Many authors have studied this instability in the context of tokamak physics (see, e.g., Shafranov 1957; Kruskal et al. 1958) and the solar corona (e.g., Gold & Hoyle 1960; Anzer 1968; Hood & Priest 1980; Mikic, Schnack, & Van Hoven 1990). In both cases, the focus has been on finding the critical twist for instability, because the kink instability is expected to be catastrophic: in a tokamak, sending the hot plasma core into the tokamak wall and destroying the confinement, and in a coronal flux tube, initiating reconnection and flaring.

In a previous paper (LLF) we investigated the linear phase of the kink instability. We derived and solved the equations for the eigenvalue problem for the linearized momentum equation

$$F_0(\xi_0) = \rho_0 \frac{d^2\xi_0}{dt^2} = \frac{J_0 \times B_1}{c} + \frac{J_1 \times B_0}{c} - \nabla p_1 , \quad (1)$$

where F_0 is the ideal MHD force per unit volume. $B_0 = (0, B_\theta, B_z)$ is the unperturbed magnetic field expressed in cylindrical coordinates, and describes a flux tube with an outer radius outside of which the field is zero. $B_1 = \nabla \times (\xi_0 \times B_0)$ is the perturbed field in Eulerian coordinates, ρ_0 is the unperturbed density, assumed constant, p_1 is the perturbed pressure, and $J = c\nabla \times B/4\pi$. The velocity has been expressed in terms of the displacement vector (ξ_0) as $v = d\xi_0/dt$.

We solved the eigenvalue problem $\rho_0 d^2\xi_0/dt^2 = \omega_0^2 \rho_0 \xi_0 = F_0(\xi_0)$, using the energy method (Bernstein et al. 1958), for cylindrically symmetric flux tubes confined by external field free plasma. We investigated tubes with constant field line pitch, i.e.,

$$\frac{B_\theta}{rB_z} = q = \text{constant} , \quad (2)$$

where q is set by the choice of equilibrium, and found analytical solutions to the eigenvalue problem for weakly twisted tubes and numerical solutions for tubes of arbitrarily large twist. This allowed us to find the displacement eigenfunctions ξ_0 and the growth rate eigenvalues ω_0 for the kink instability of any constant-twist magnetic flux tube. Our results agreed with the analysis of Roberts (1956),

who considered uniform axial fields, and Goedbloed & Hagebeuk (1972), who considered equilibria quite similar to ours, but only in our "weakly twisted" limit. The eigenvalues and eigenfunctions are related by the expression

$$\omega_0^2 = \frac{\int d^3x \xi_0^* F_0}{\int d^3x \rho_0 |\xi_0|^2} = \frac{\int d^3x [\xi_0^* \cdot (\nabla \times B_0) \times B_1 - |B_1|^2]}{4\pi\rho_0 \int d^3x |\xi_0|^2} . \quad (3)$$

This formulation assumes incompressible flow and zero viscosity and magnetic resistivity.

The main results are as follows. These constant-twist equilibria are unstable if the field-line pitch exceeds a threshold, $q \geq q_{cr}$. The threshold is $q_{cr} = a^{1/2}$, where a is the r^2 coefficient in the Taylor series expansion of the equilibrium axial magnetic field (B_z) about the tube axis ($r = 0$): $B_z(r) = B_0(1 - ar^2 + \cdots)$. When this criterion is violated, there are unstable helical eigenmodes, $\xi_0 \propto e^{i(\theta + kz) + \omega_0 t}$. The most unstable of these have a helical pitch $-k$, which is near (but not equal to) the field-line pitch q. The maximum growth rate and range of unstable wavenumbers for a strongly twisted tube can be predicted qualitatively by using the analytical results from the weakly twisted case. The maximum growth rate in that case is given by $\omega_{0,\max} = v_A R(q^2 - q_{cr}^2)/3.83$, where v_A is the Alfvén speed on axis. The range of unstable wavenumbers is $(-q - \Delta k/2) < k < (-q + \Delta k/2)$, where $\Delta k = 4qR(q^2 - q_{cr}^2)^{1/2}/3.83$.

4. SETTING UP THE NONLINEAR SIMULATIONS

4.1. *Governing Equations*

The governing equations for this three-dimensional, compressible, dissipative MHD system are (as adapted from Dahlburg & Norton 1995)

$$\frac{\partial \rho}{\partial t} = -\nabla \cdot (\rho v) , \quad (4)$$

$$\rho \frac{Dv}{Dt} = \frac{J \times B}{c} - \nabla p + \mu \nabla \cdot \tau , \quad (5)$$

$$\frac{\partial B}{\partial t} = \nabla \times (v \times B) + \eta \nabla^2 B , \quad (6)$$

$$\frac{\partial U}{\partial t} = -\nabla \cdot (Uv) - p\nabla \cdot v + \mu\tau \cdot \nabla v + \kappa\nabla^2 T + \frac{4\pi\eta}{c^2}|J|^2 , \quad (7)$$

$$p = (\gamma - 1)U , \quad (8)$$

$$\nabla \cdot B = 0 . \quad (9)$$

Here we define $\rho(x, t)$ as the mass density, $v(x, t)$ as the flow velocity, $p(x, t)$ as the plasma pressure, $B(x, t)$ as the magnetic induction field, $U(x, t)$ as the internal energy density, $T(x, t) = \gamma U/\rho C_p$ as the temperature, and $\tau_{i,j}(x, t) = (\partial_j v_i + \partial_i v_j) - \frac{2}{3}\nabla \cdot v\delta_{ij}$ as the viscous stress tensor; $\gamma = 5/3$ is the adiabatic ratio, C_p is the specific heat at constant pressure, and c is the speed of light. The thermal conductivity (κ), magnetic resistivity (η) and viscosity (μ) are constant and uniform, and the Stokes relationship is assumed (see, e.g., Panton 1996, p. 131). The important dimensionless numbers are $S_v = \rho_0 v_A L_0/\mu \equiv$ the viscous Lundquist number, $S_r = v_A L_0/\eta \equiv$ the resistive Lundquist number,

and $\beta = 8\pi p_0/B_0^2 \equiv$ the ratio of plasma to magnetic pressure. In these definitions, ρ_0 is a characteristic density, $v_A = B_0/(4\pi\rho_0)^{1/2}$ is the Alfvén speed, L_0 is a characteristic length (the tube radius R), and p_0 and B_0 are characteristic pressure and magnetic field strength, taken as the initial values at the center of the flux tube.

4.2. Initial Equilibrium

For the present simulations we concentrate on constant twist flux tubes of the form [in cylindrical coordinates (r, θ, z)]

$$B_z = B_0(1 - r^2/R^2)^p , \quad B_\theta = qrB_z , \quad (10)$$

for $r \le R$, and $\mathbf{B} = 0$ for $r > R$. This profile has been chosen to make the magnetic field go smoothly to zero at the outer radius of the tube, $R = \pi/4$. The tube is contained in a periodic simulation box of side $L = 2\pi$ (see Fig. 2). The exponent p allows us to vary the rate at which the magnetic field drops off with radius. As noted in § 3, these tubes will be unstable when $qR > p^{1/2}$, and the growth rate will vary as $\omega_0 R/v_A \sim (q^2 R^2 - p)$. Note that this equilibrium is not necessarily force-free: radial pressure gradients are required for force balance, and we initialize the pressure appropriately so that the tube is initially in equilibrium. Pressure gradients are expected to play a role in convection zone flux tubes because of the high ratio of plasma pressure to magnetic pressure: $\beta \gtrsim 10^4$. Very minor changes in pressure are therefore sufficient to balance magnetic forces. The plasma β in our simulation is about 600, so the plasma motion will be nearly incompressible, as is expected for the convection zone. The Lundquist numbers are $S_v = 10^2$ and $S_r = 10^5$. Thus both Lundquist numbers are much greater than unity, as they are expected to be in the convection zone. Viscosity and resistivity will therefore play only a small role for the dynamical timescales of interest.

4.3. Initial Perturbation

To excite the kink instability, we initialize the simulation with a helically symmetric velocity perturbation with a magnitude $v_A/140$. The straight equilibrium flux tube is perturbed with an initial velocity based on the weakly twisted analytic approximation of the eigenmode. While not the exact eigenmode, it is sufficiently close to excite the kink instability.

4.4. Code

The simulations are performed on the Naval Research Laboratory's connection machine CM5E using a massively parallel algorithm. The numerical code solves the three-dimensional compressible visco-resistive MHD equations with triply periodic boundary conditions. A description of the code can be found in Dahlburg & Norton (1995). The MHD variables are advanced by a de-aliased three-dimensional Fourier collocation method with 128^3 Fourier modes (see Dahlburg & Picone 1989). Time is advanced using the second-order Runge-Kutta method, with a Courant condition set by

$$\frac{\delta t}{\delta x} \max \left[\Sigma(|v| + v_A + c_s) \right] < 0.3 , \quad (11)$$

where δt is the time step, and δx is the collocation point grid spacing. To prevent the occurrence of the Gibbs phenomenon when sharp features are Fourier discretized (e.g., magnetic field profiles with very small p), the initial conditions are passed through a raised cosine filter (see, e.g., Canuto et al. 1987). For these 128^3 Fourier mode simulations, 105 GB of parallel storage and 5 s per time step are used on the NRL CM5E. The code has previously been used to explore magnetic flux tube reconnection and interaction (Dahlburg & Antiochos 1997) and magnetic flux tube tunneling, a multiple reconnection process by which one flux tube can pass through another (Dahlburg, Antiochos, & Norton 1997; Antiochos & Dahlburg 1997).[4]

5. RESULTS

5.1. Outline of Goals

We want to understand, in as general a way as possible, what happens to kink-unstable flux tubes. While we restrict ourselves to constant-twist tubes, we make an effort to study those tubes as completely as possible. From linear analysis we found that the growth rate and eigenfunction depend on twist (q) and the radial variation of B_z, which in our case is parameterized by p (see eq. [10]). The equilibria thus have two free parameters, p representing the field gradient, and q representing field-line pitch. Because of time limitations, we could not completely cover parameter space, but as a compromise we chose three values of q and three values of p and performed nine simulations corresponding to those values. We also performed two additional p and q pairs and a Gold-Hoyle field (see eq. [31]), as this is a special case of the constant-twist field—the force-free constant-twist field—and has received much attention in the literature. For each simulation, k was chosen as the integer that gives the maximum growth rate for the tube profile; k has to be an integer so that an integral number of
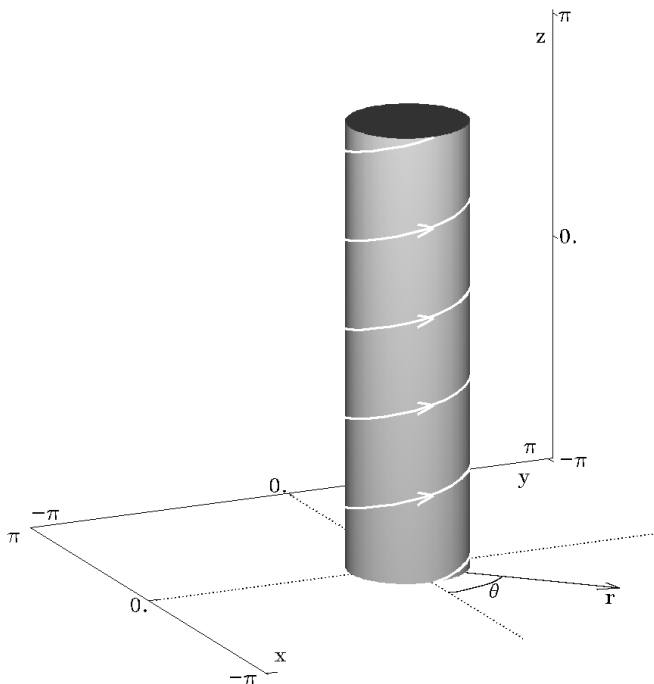

FIG. 2.—Isosurface of initial flux tube in simulation box. The isosurface is for run 2 (see Table 1) at half the maximum field. A representative field line is drawn on the surface of the tube, with $q = 5$ for this run.

wavelengths fits into the periodic simulation box. The values of p chosen vary from 0.1 to 1, giving a good representation of B_z profiles ranging from nearly square ($p = 0.1$) to parabolic ($p = 1$). The values of q, varying from 2.5 to 7.5, were chosen to give a range of twist that was large enough to give reasonably fast growth rates and small enough to keep k low. As the kinks we excited were periodic, all information about them is contained within one wavelength. We therefore chose to look at a small number of wavelengths (low k) with high resolution rather than a large number (high k) with low resolution. For each simulation we compare the linear phase with the predicted linear behavior from LLF; we find the time for saturation of each tube; and we characterize the saturation equilibrium of each tube.

5.2. Linear Phase

For all 12 simulations, the expected instability was indeed excited. Figure 3 shows the kinetic and magnetic energy of a typical simulation, denoted run 2 in Table 1. The kinetic energy increases exponentially early in the simulation when
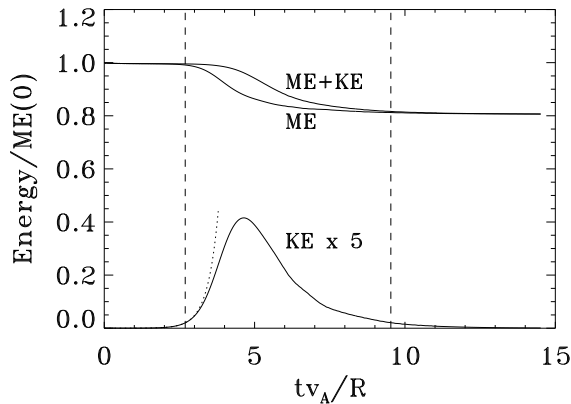

FIG. 3.—Magnetic energy (ME), kinetic energy (KE), and the sum of the two (ME + KE) vs. time for run 2. The kinetic energy has been multiplied by 5 to make it visible on the same scale as the magnetic energy. The dotted line shows the exponential fit to the linear phase. The two dashed lines show the times at which the kinetic energy first increases above, and last decreases below 5% of the maximum. These two times are used to define the saturation time.

the instability is in its linear phase, peaks, and then decreases to zero as the instability saturates. This same qualitative behavior occurs in all the simulations. When the time evolution of the kinetic energy is plotted on a linear-log scale, the initial exponential increase appears as a straight line. We measure the slope of this line to find the growth rate ω of the linear phase of the instability. This measured exponential growth curve for run 2 is plotted as the dotted line on Figure 3. The time axis in this plot is measured in units of R/v_A, where v_A is the initial Alfvén speed of the tube on its axis.

Figure 4 shows the axial ($\hat{z}$) velocity of the tube in a horizontal plane ($z = 0$) during the linear phase of run 2 compared to the predicted velocity. Figure 5 compares the radial profiles of the predicted velocities with those from the linear phase of run 2: v_r, which varies as $\cos(kz + \theta)$, at $kz + \theta = 0$; and v_θ and v_z, which vary as $\sin(kz + \theta)$, at $kz + \theta = \pi/2$. In both cases one can see that the linear phase is predicted very well by our theory. The wavenumber of the nonlinearly simulated kink is the same as that predicted, and even in the nonlinear phase of development, the tube is helically symmetric (except for a small amount of noise: e.g., typically the helical $m = 0$ plus $m = 1$ components [see below] of B_z differ from the total B_z by less than 5% of the maximum of B_z).

The predicted ideal growth rates from our linear theory (ω_0: eq. [3]) for all runs and the corresponding simulation growth rates, measured as described above, are compared in Figure 6, where they are plotted as plus signs. The ideal growth rates are consistently higher than the simulation growth rates, varying from a factor of 1.1 to 1.9, with an rms error in $(\omega_0 - \omega)/\omega$ of 40%. This is to be expected, since the code includes viscosity which will decrease the growth rates below their ideal values. (The resistivity is too small to affect the growth rates significantly.)

To account for the effects of viscosity using our linear analysis (see eq. [3]), we now consider the viscous force for incompressible flow:

$$F_1 = \mu \nabla^2 v , \qquad (12)$$

as a first-order perturbation on the ideal force F_0. Here μ is the explicit viscosity of the code. We use F_1 to find the

TABLE 1

KINK SIMULATION PARAMETERS AND RESULTS

Run	p	q	k	$\omega_0 R/v_A$	$\Delta x/R$	$\bar{\alpha}_0 R$	$\delta\alpha_0$	$\delta\alpha_1$	$\delta\alpha_i$
1	1	2.5	−2	0.345	0.024	3.11	0.133	0.276	0.293
2	1	5	−3	1.54	0.145	2.90	0.074	0.258	0.639
3	1	7.5	−4	2.91	0.154	2.42	0.064	0.182	0.923
4	0.5	2.5	−2	0.474	0.050	2.94	0.072	0.307	0.295
5	0.5	5	−3	1.82	0.172	2.76	0.033	0.203	0.664
6	0.5	7.5	−4	3.32	0.172	2.36	0.085	0.220	0.948
7	0.25	1.5	−1	0.198	0.094	2.87	0.036	4.07	0.343
8	0.25	2.5	−2	0.583	0.055	2.76	0.046	0.295	0.439
9	0.25	5	−3	2.06	0.178	2.29	0.034	0.190	0.747
10	0.25	7.5	−4	3.65	0.159	1.74	0.090	0.297	1.03
11	0.1	4	−2	1.59	0.344	2.19	0.025	0.324	0.761
G-H[a]......	...	3	−2	0.267	0.021	4.79	0.241	0.195	0.368

NOTE.—p is the initial field profile parameter defined in eq. (10), q is the twist parameter, k is the wavenumber of the instability, ω_0 is the growth rate predicted from the linear theory, Δx is the magnetic field–weighted horizontal displacement of the final equilibrium, and $\bar{\alpha}$ is the area average over $r < 2R/3$ of α calculated from the $m = 0$ components of the final field and current; $\delta\alpha$ is the standard deviation of α, calculated as in eq. (26), for the final $m = 0$ field ($\delta\alpha_0$), the final $m = 1$ field ($\delta\alpha_1$), and the initial field ($\delta\alpha_i$).

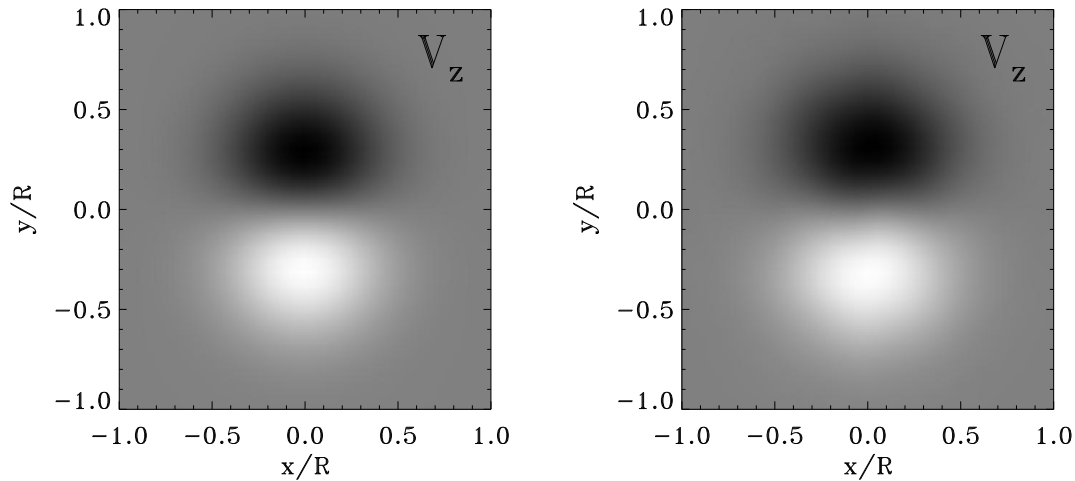[a] Note that R for the Gold-Hoyle tube is twice that of the other tubes.

FIG. 4.—$\hat{z}$ velocity in a $z = 0$ slice of the tube for the linear phase of run 2 (*right*) compared to the velocity predicted by the stability theory (*left*). The shading represents the strength of v_z. Negative velocities are shown as black, and positive velocities as white.

first-order correction to the growth rate using perturbation theory (see, e.g., Courant & Hilbert 1989). The force, growth rate squared (eigenvalue), and displacement (eigenfunction) are all expanded to first order:

$$F = F_0 + F_1 + \cdots , \qquad (13)$$

$$\omega_\mu^2 = \omega_0^2 + \omega_1^2 + \cdots , \qquad (14)$$

$$\xi = \xi_0 + \xi_1 + \cdots . \qquad (15)$$

Substituting these expanded variables into the eigenfunction equation $F(\xi) = \rho_0 \omega_\mu^2 \xi$ and keeping terms up to first order, we find

$$F_0(\xi_0) + F_1(\xi_0) + F_0(\xi_1) = \rho_0(\omega_0^2 \xi_0 + \omega_1^2 \xi_0 + \omega_0^2 \xi_1) . \qquad (16)$$

We next multiply by ξ_0^* and integrate over all space. The zeroth-order terms cancel (eq. [3]), and leave

$$\int d^3x \xi_0^* \cdot F_1(\xi_0) + \int d^3x \xi_0^* \cdot F_0(\xi_1)$$

$$= \rho_0 \omega_1^2 \int d^3x \, |\xi_0|^2 + \rho_0 \omega_0^2 \int d^3x \xi_0^* \cdot \xi_1 . \qquad (17)$$

Using the fact that F_0 is self-adjoint, and the fact that ω_0^2 is real (see Freidberg 1987, p. 242) we can rewrite the second term on the left-hand side:

$$\int d^3x \xi_0^* \cdot F_0(\xi_1) = \int d^3x \xi_1 \cdot F_0(\xi_0^*) = \rho_0 \omega_0^2 \int d^3x \xi_1 \cdot \xi_0 . \qquad (18)$$
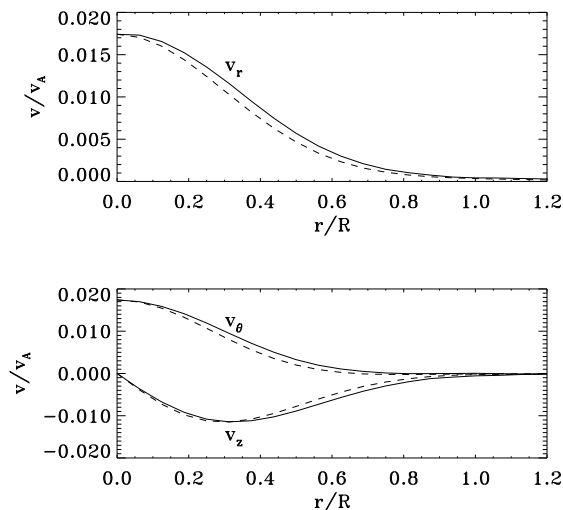

FIG. 5.—Radial, axial, and azimuthal velocities during the linear phase of run 2 (*solid lines*) compared with the velocities predicted by the linear theory (*dashed lines*). The theoretical velocities were scaled so that the maximum of v_r coincided with that of the simulation. Note that v_r varies as $\cos(kz + \theta)$, while v_θ and v_z vary as $\sin(kz + \theta)$.
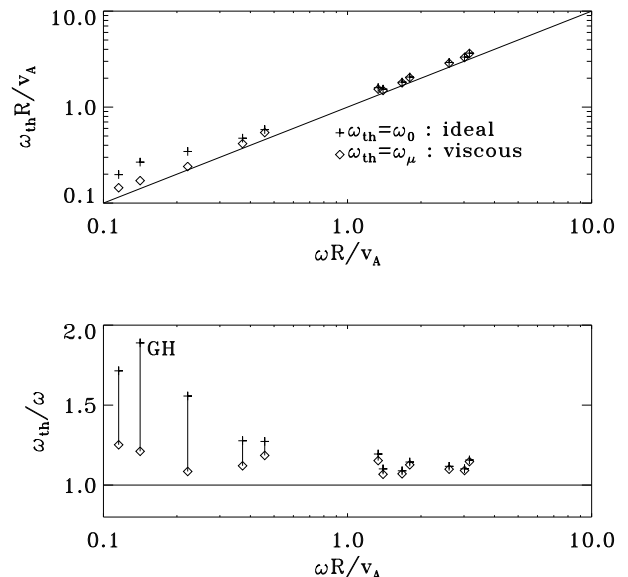

FIG. 6.—Comparison of the theoretical growth rates ω_{th} with the growth rates ω measured from the simulations. The theoretical growth rates are calculated from the linear theory. The ideal growth rates are calculated from eq. (3), and the viscous growth rates are calculated from eq. (20). The Gold-Hoyle simulation is marked GH in the second panel.

This term cancels with the second term on the right-hand side of equation (17), and we can solve for the first-order correction to the growth rate,

$$\omega_1^2 = \frac{\int d^3x \boldsymbol{\xi}_0^* \cdot \boldsymbol{F}_1(\boldsymbol{\xi}_0)}{\int d^3x \rho_0 |\boldsymbol{\xi}_0|^2} . \tag{19}$$

Writing $\boldsymbol{F}_1(\boldsymbol{\xi}_0) = \nabla^2 \boldsymbol{v}(\boldsymbol{\xi}_0) = \omega_0 \nabla^2 \boldsymbol{\xi}_0$, this becomes

$$\omega_1^2 = -\mu\omega_0 \frac{\int d^3x |\nabla \times \boldsymbol{\xi}_0|^2}{\int d^3x \rho_0 |\boldsymbol{\xi}_0|^2} . \tag{20}$$

This first-order correction reduces the predicted growth rate below the ideal value. Using this formulation, we calculate the reduced growth rates and plot them against the measured growth rates as diamonds in Figure 6. One can see that these explicit viscous effects account for a significant part of the discrepancy between the predicted and measured growth rates, with the rms error now at 15% for a variation of growth rates of over a factor of 30. This indicates that our linear calculations from the energy method explain the linear phase of our simulation quite well. The remaining error may be due to numerical errors caused by the finite number of Fourier modes used in the spectral calculations.

5.3. Nonlinear Phase

After several Alfvén crossing times, the instability leaves the linear phase, as indicated by the deviation of the kinetic energy from exponential growth (see Fig. 3). The instability soon peaks at a level that can be predicted by the initial azimuthal magnetic energy, as shown in Figure 7.

After reaching its peak, the kinetic energy then decreases, in some runs oscillating several times, but always approaching zero, indicating that the instability has saturated and the tube has found a new stable equilibrium. An investigation of the energy balance throughout the simulation shows that the instability converts magnetic energy into kinetic energy, and this is then converted into internal energy through viscous dissipation. There is also a conversion of magnetic energy directly into internal energy through ohmic dissipation. (We found the energy exchange due to pressure work to be negligible.) This ohmic dissipation is insignificant for the more unstable runs but is quite significant for the weakly unstable runs (for example, it accounts

for less than 1% of the magnetic energy loss in run 10 but accounts for 55% of the magnetic energy loss in run 7). For all runs the ohmic dissipation occurs at a steady rate throughout the simulation and therefore appears to be unaffected by the instability. This means the kink is not causing the tube to form current sheets where enhanced reconnection would take place, and the tube topology is therefore not being changed. This final state is different from the nonlinear kink simulations which have been performed on variable twist tubes by Baty (1996) and Craig & Sneyd (1990). These studies find purely internal kinks, meaning kinks confined within the mode-resonant surface where the local twist equals the kink wavenumber. They find that current concentrations or sheets are generated at this mode-resonant surface, allowing reconnection to occur. As we do not have a mode-resonant surface, we do not find purely internal kinks or the associated current sheets and reconnection.

Figure 8 shows an isosurface of the final equilibrium for run 2. The surface shown is that at which the magnitude of the magnetic field is half of the maximum. This clearly shows that this equilibrium is a kinked equilibrium with the expected wavenumber, $|k| = 3$, and that the pitch of the kink is in the same sense as the initial field-line pitch, shown in Figure 2. Again, while the tube has definitely kinked, it has not kinked so severely as to fold over on itself and initiate reconnection.

One measure of the kink amplitude is the field-strength–weighted first moment of the tube cross section, defined as

$$\Delta x \equiv \left| \frac{\int dA |\boldsymbol{B}| x}{\int dA |\boldsymbol{B}|} \right| . \tag{21}$$

The top panel of Figure 9 shows the amplitude of this moment at saturation for each of the runs. While the kink
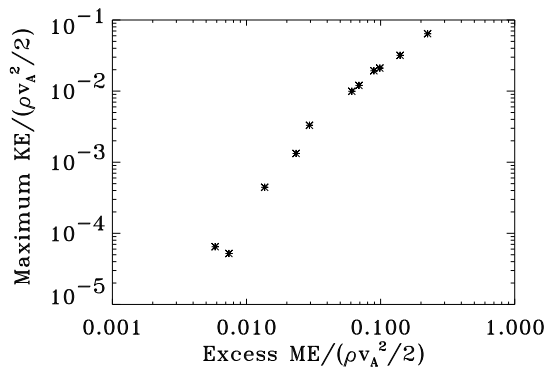

FIG. 7.—Maximum kinetic energy density of the instability vs. excess initial azimuthal magnetic energy density for each simulation. The excess azimuthal energy is calculated by subtracting the azimuthal magnetic energy of the marginally stable tube with the same B_z profile and $q = q_{cr}$, as calculated from the stability theory, from the initial azimuthal magnetic energy. The Gold-Hoyle tube is not plotted, as $q = q_{cr}$ for this profile, giving an excess azimuthal energy of zero.
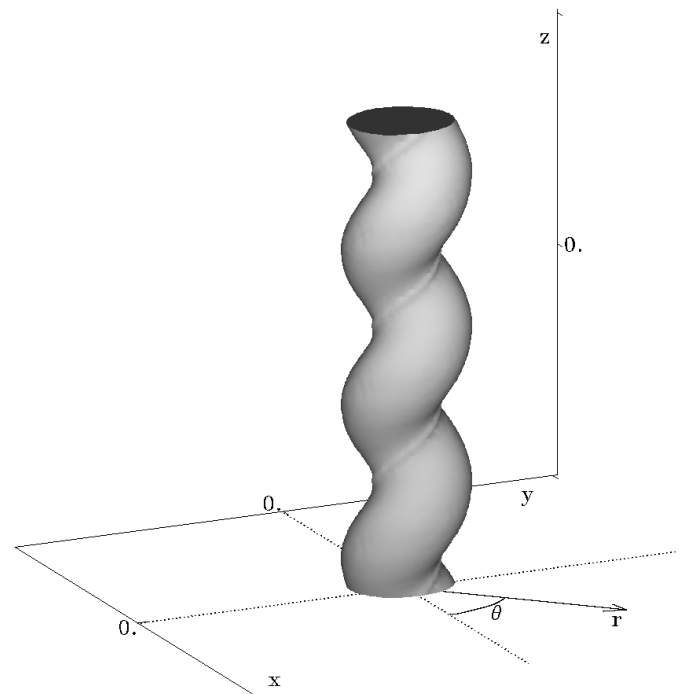

FIG. 8.—Isosurface of $|\boldsymbol{B}|$ for run 2. The surface shown is the surface where the magnetic field strength is half the maximum field strength. It can be seen that three wavelengths of the kink are included in the simulation box, indicating that $|k| = 3$.
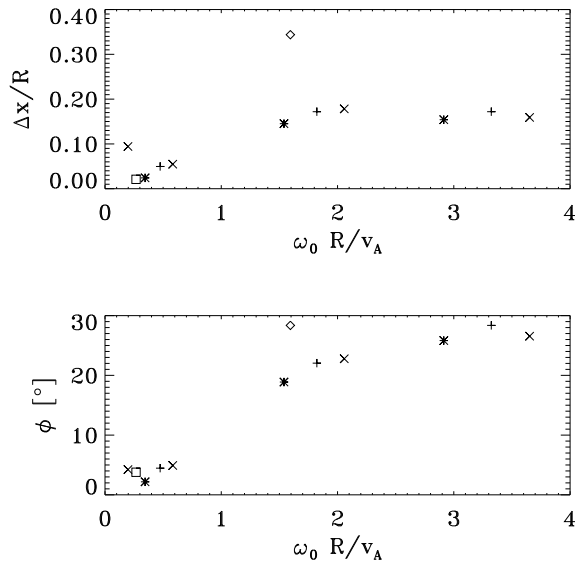
FIG. 9.—Final horizontal displacement of each of the simulations vs. growth rate (*upper panel*), and the corresponding initial angle of emergence (*lower panel*). The angle is defined as $\phi = \arctan(\Delta x |k|)$ (see text). Asterisks are for $p = 1$, plus signs for $p = 0.5$, crosses for $p = 0.25$, the diamond for $p = 0.1$, and the square for the Gold-Hoyle tube.

amplitudes are only a fraction ($<40\%$) of the tube radius, they are large enough to have a significant effect on the tube geometries. To calculate the maximum degree by which a kink instability could tilt the axis of a tube with respect to its initial position, we return to the picture of a kinking Ω-loop in Figure 1. We project the tube onto a horizontal plane (as is done at the bottom of this figure), defined as the x-z plane, where the original axis of the tube lies on the z-axis. Within this plane, the kink displaces the axis of the tube in the x-direction. The new x location of the axis becomes

$$x = \Delta x \sin(kz) . \tag{22}$$

Similarly, the vertical displacement becomes $y = \Delta x \cos(kz)$. At the apex, $z = 0$, of the Ω-loop the x displacement of the axis is zero, and the tilt of the tube axis with respect to the z-axis is at a maximum. The angle of tilt ϕ at $z = 0$ can be estimated as

$$\tan \phi \equiv \frac{dx}{dz}\bigg|_{z=0} = k \Delta x . \tag{23}$$

Knowing Δx and k, we can calculate ϕ, and this is plotted in the bottom panel of Figure 9. There is only a qualitative relationship between equation (23) and the tilt angle an actual kinked flux tube might form, but it is nevertheless very illustrative of what that angle might be. The maximum angle achieved in our simulations is $\sim 30°$, with the trend being that tubes with larger growth rates become kinked with larger angles. This can be interpreted as a 30° deviation from the normal tilt a tube would have with respect to the equator on emergence through the photosphere, and thus supports the theory that a kink instability is responsible for the unusual tilt angles of δ-spots.

Figures 10 and 11 follow the evolution of the axial magnetic field B_z and perpendicular magnetic field $|B_\perp|$ in the $z = 0$ plane, as the tube goes from the linear phase to saturation. The profiles in these figures start out cylindrically symmetric. As the instability evolves, the helical deforma-

tion of the tube moves the profile to the right. At the peak of its displacement, corresponding to the peak in the kink amplitude plot, the profile takes on a kidney bean shape. It then rebounds and eventually settles down in a more oval or D-shaped equilibrium displaced to the right of the initial equilibrium. Note that these displacements represent helical displacements of the tube: the direction of the displacement will rotate as $kz + \theta$ if a different z cross section is taken.

The helical deformation is also shown by the tilt of the tube. While this cannot be seen directly in these figures, the effect of this tilt on the B_z profile is evident: a white crescent soon appears at the right edge of the tube. This indicates that negative field has appeared where there was none before. This is not the result of reconnection but rather the result of the tilt of the tube axis: the B_θ component of the initial field, upon being tilted, adds to the B_z component of the field. The right-handed azimuthal field therefore creates negative axial field at the right edge of the tube. Figure 12 shows the B_z, B_y, and B_x profiles on the x-axis at $z = 0$. The evolution of the B_z profile clearly shows how the tube is strongly perturbed at the beginning, extends beyond the eventual kinked equilibrium, and then rebounds to settle into the final equilibrium.

Figure 13 shows the saturation time for each of the runs versus the linear e-folding time ($1/\omega_0$). The saturation time is defined as the elapsed time from when the kinetic energy first increases above 5% of its maximum value to when it last decreases below 5% of the maximum. These two times are shown for run 2 on Figure 3 as the two vertical dashed lines. There is a clear linear relationship between the saturation time and the linear e-folding time, with the tubes (excluding the Gold-Hoyle tube) taking about 10 e-folding times to saturate. *This general result allows us to predict kink saturation timescales solely from a knowledge of the initial equilibrium.*

5.4. *Final Equilibrium Configuration*

The final equilibrium field for these tubes is generally more force-free than the initial one (with the exception of the Gold-Hoyle tube, which is force-free to begin with). A force-free field can be written in the general form

$$\nabla \times \boldsymbol{B} = \alpha \boldsymbol{B} , \tag{24}$$

where α is a function of $\boldsymbol{x}$. This ensures that $\boldsymbol{J} \times \boldsymbol{B}$ is zero. We looked at $\alpha \equiv (\nabla \times \boldsymbol{B}) \cdot \boldsymbol{B}/|\boldsymbol{B}|^2$ and found that in addition to the field becoming more force-free, the distribution of α across the tube becomes somewhat more uniform. This suggests that the tube might be evolving to a helically symmetric force-free constant-α equilibrium, although, as we show below, this is not precisely true. Helically symmetric constant-α force-free fields are given by the "Chandrasekhar-Kendall" functions $\boldsymbol{B}_m(r, \psi)$ (Chandrasekhar & Kendall 1957; Taylor 1986). Each $\boldsymbol{B}_m$ is a solution of equation (24) with uniform α and depends on ψ as $m\psi$, where m is an integer and

$$\psi = kz + \theta . \tag{25}$$

We decomposed the final equilibrium field into its m components by Fourier transformation, and found they consisted of the $m = 0$ cylindrically symmetric component and the $m = 1$ helically symmetric component.

Before comparing the equilibrium fields with the Chandrasekhar-Kendall functions, we investigated the force-free, constant-α nature of the $m = 0$ and $m = 1$ com-
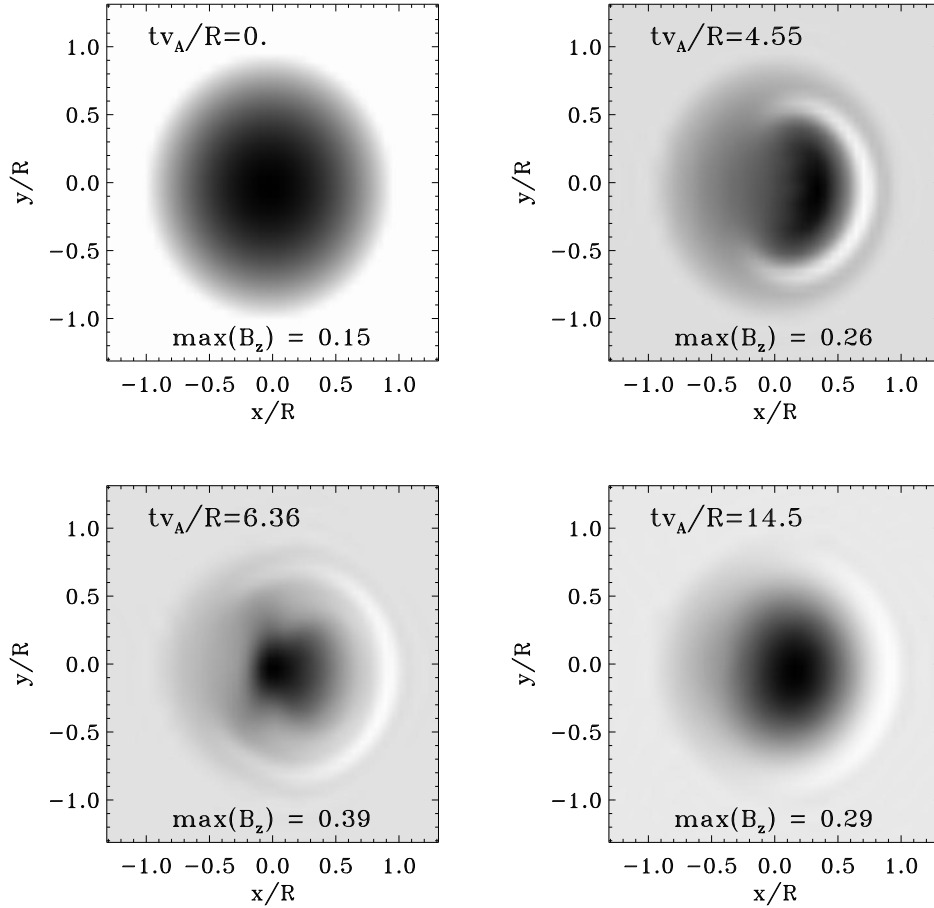
FIG. 10.—Slices of axial magnetic field B_z at $z = 0$ at various times during the instability for run 2. The instability has saturated by the last frame. The shading represents the strength of B_z. Black represents positive field, and white represents negative field.

ponents of the fields separately. Figure 14 compares the components of J parallel and perpendicular to B as a function of radius for the initial equilibrium field and the $m = 0$ and $m = 1$ components of the final equilibrium field of run 2. This shows that while there is a significant $J \times B$ force in the initial equilibrium (balanced by pressure forces), the final $m = 0$ and $m = 1$ equilibria are largely force-free. The only significant forces in the final equilibrium are at the outer edge of the tube where magnetic forces are required to balance the excess external pressure.

Figure 15 shows the radial profile of α for the initial profile and the $m = 0$ and $m = 1$ components of the final profile. This shows that while the initial α profile varies significantly with radius, the final α profile for the $m = 0$ component of the field is relatively constant. Thus the cylindrically symmetric part of the final equilibrium appears to be a force-free, constant-α field. This holds in general for all the p-profile tubes studied, as is shown in Table 1, which tabulates the mean values of α for the inner two-thirds of each tube and also shows the standard deviation of α. This normalized standard deviation is defined as

$$\delta\alpha \equiv \sqrt{\frac{\int dA[\alpha(r, \theta) - \bar{\alpha}]^2}{\bar{\alpha}^2 A}}, \qquad (26)$$

where the integration is over the area inside a radius of $r = 2R/3$, and $\bar{\alpha}$ is the average value of α over the same area. A comparison of the final $\delta\alpha$ with the initial value (Table 1) shows how much more uniform α becomes when the tube

kinks. The final $m = 1$ α-profile in Figure 15 and the tabulated values of $\delta\alpha$ for $m = 1$ show that, in contrast to the $m = 0$ field, the $m = 1$ field does not have a uniform value of α. There appears, therefore, to be a significant difference between the behaviors of the $m = 0$ and $m = 1$ modes.

The $m = 0$ Chandrasekhar-Kendall function is also called the Lundquist field (Lundquist 1951) and is written as

$$B_z = B_0 J_0(\alpha r), \quad B_\theta = B_0 J_1(\alpha r). \qquad (27)$$

This solution is compared to the $m = 0$ part of the kinked equilibrium field of run 2 in Figure 16. B_0 has been set here to match the amplitude of the simulation B_z at $r = 0$, and α has been taken to be $\bar{\alpha} = 2.90/R$. The top panel of Figure 16 shows that the two magnetic field profiles agree quite well everywhere but at the edge of the tube. The bottom panel of Figure 16 shows, however, that the $m = 1$ Chandrasekhar-Kendall function solution does not match the $m = 1$ equilibrium field.

The $m = 1$ mode behavior can be explained in a qualitative way by noting that the helicity of each field line is approximately conserved (in an ideal MHD tube, where the magnetic diffusivity is zero, the local helicity would be exactly conserved). Initially, each field line in a constant-twist tube has the same helicity (e.g., helicity $= q = 5$ for run 2). If reconnection does not play a large part in the evolution, one expects the helicity to be the same for each field line at the end of the simulation. To investigate this, we first define the coordinate s as the distance along the field line and the vector $X(s)$ as the vector position of the field
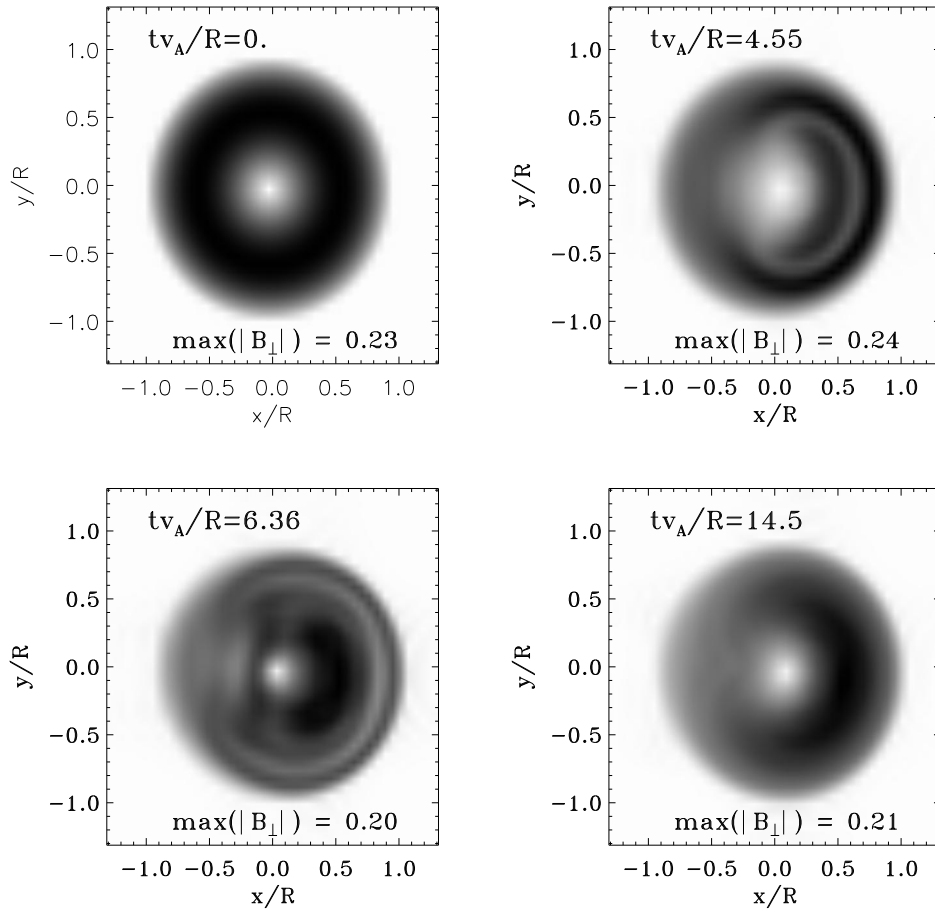
FIG. 11.—Slices of perpendicular magnetic field $|\boldsymbol{B}_\perp|$ at $z = 0$ at various times for run 2. The shading represents the magnitude of the magnetic field perpendicular to the z-axis, with zero field being white.
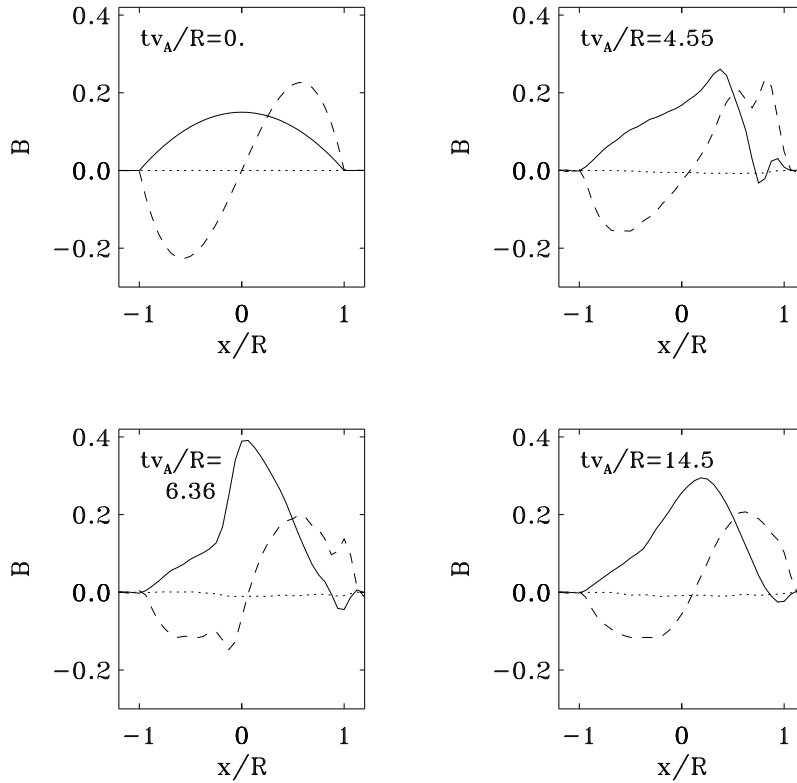

FIG. 12.—Profiles of B_z (*solid line*), B_y (*dashed line*), and B_x (*dotted line*) on the x-axis at $z = 0$ at various times during the instability for run 2
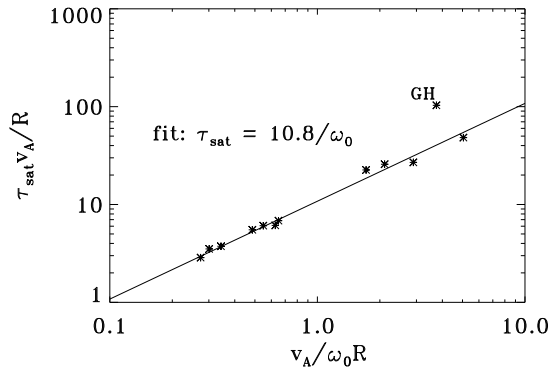
FIG. 13.—Saturation time τ_{sat} vs. e-folding time $1/\omega_0$. The saturation time is defined as the time from when the kinetic energy first increases above 5% of the eventual maximum to the time when the kinetic energy last decreases below 5% of the maximum. See Fig. 3. The Gold-Hoyle field is not included in the fit.
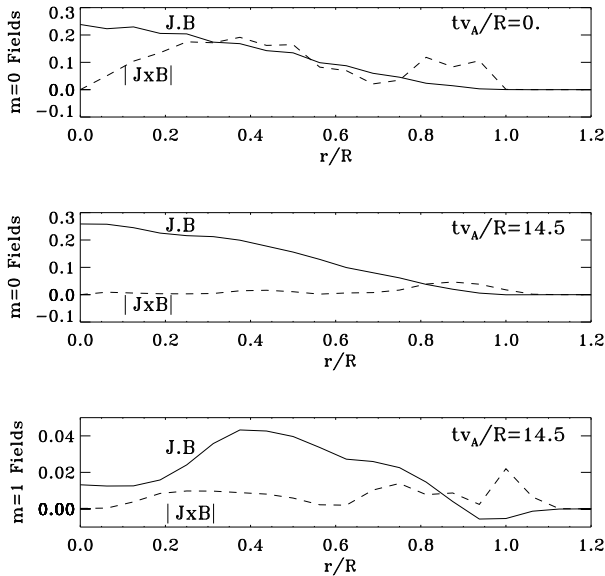

FIG. 14.—Comparisons of J parallel and perpendicular to B as a function of radius for the initial equilibrium and for the cylindrically symmetric ($m = 0$) and helically symmetric ($m = 1$) parts of the final equilibrium. This shows that both the $m = 0$ and $m = 1$ parts of the final equilibrium are largely force-free. The $m = 1$ profile is taken at $kz + \theta = 0$.
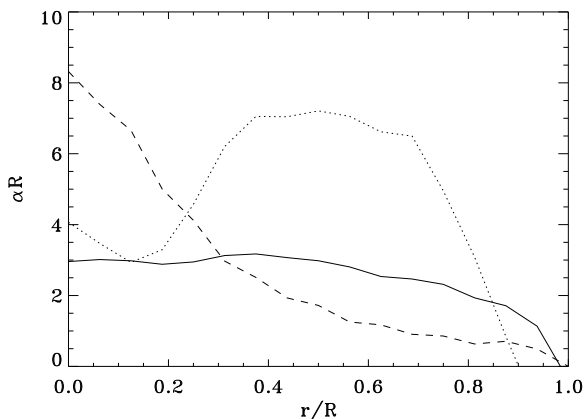

FIG. 15.—Profiles of the force-free parameter α for the initial field (dashed line) and the $m = 0$ (solid line) and $m = 1$ (dotted line) components of the final field of run 2; α for $m = 1$ is shown at $kz + \theta = 0$.
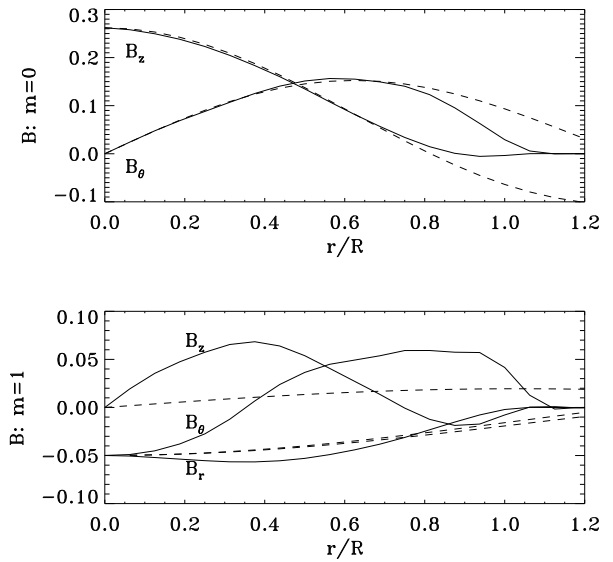

FIG. 16.—Final field equilibrium components, $m = 0$ and $m = 1$ (solid lines), compared to the Chandrasekhar-Kendall fits (dashed lines). It is clear that the $m = 0$ Chandrasekhar-Kendall function (eq. [27]) fits the $m = 0$ equilibrium quite well, while the $m = 1$ Chandrasekhar-Kendall function does not fit the $m = 1$ equilibrium. Note that the $m = 1$ components of B_z and B_θ vary as $\cos(kz + \theta)$, while B_r varies as $\sin(kz + \theta)$. This explains why B_x, in Fig. 12, at $kz + \theta = 0$ is essentially zero.

line at s with respect to the origin of coordinates. We then calculate the helicity of each field line as the sum of the field-line twist (Tw) and the field line writhe (Wr). The writhe is defined as

$$\mathrm{Wr}\,(X) \equiv \frac{1}{4\pi} \int_0^L \int_{-\infty}^{+\infty} ds\,ds' \, \frac{\hat{t}(s) \times \hat{t}(s') \cdot [X(s) - X(s')]}{|X(s) - X(s')|^3} \tag{28}$$

(see, e.g., Longcope & Klapper 1997). This is integrated over the same field line twice, and $\hat{t}(s)$ is the unit tangent vector at s. The limits on the first integral go only from zero to L because we are calculating the writhe per length of the simulation box rather than of the whole (infinitely long) field line. The second writhe integral extends to infinity because the writhe of any section of field line is affected by the location of the entire field line. In practice, since this effect drops off as $1/\text{distance}^2$, we only calculated the second integral from $-2L$ to $3L$. We tested this abbreviated integral on perfectly helical field lines, where Wr (X) is known analytically, and found that the calculated values of Wr differed from the true values by less than 1%.

The twist of a ribbon defined by the curve $X(s)$ and a unit spanwise normal vector $\hat{N}(s)$ (i.e., the vector lying within the ribbon and normal to its axis) is given by

$$\mathrm{Tw} \equiv \frac{1}{2\pi} \int_0^L ds \hat{N} \times \frac{d\hat{N}}{ds} \cdot \hat{t} . \tag{29}$$

For a thin flux tube Moffatt & Ricca (1992) have shown that the sum of Tw and Wr is the helicity. However this is difficult to prove for a general flux tube, and $\hat{N}(s)$ is difficult to define for a general field. We therefore use a proxy for the twist:

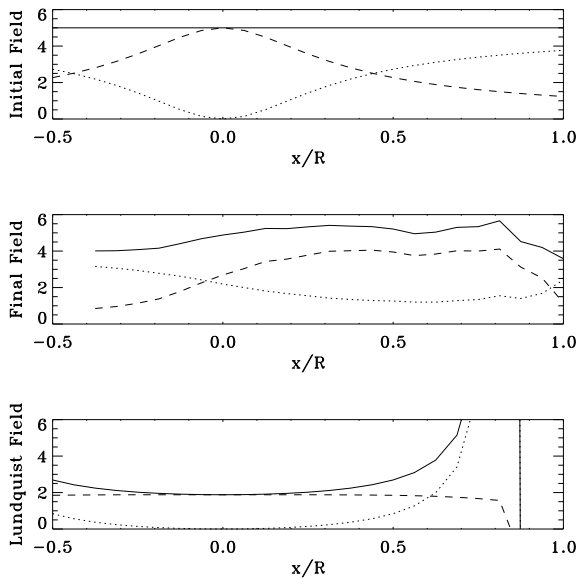$$\mathrm{Tw}\,(X) \equiv \frac{1}{c} \int_0^L ds \, \frac{J \cdot B}{|B^2|} . \tag{30}$$

FIG. 17.—Twist (*dashed line*), writhe (*dotted line*), and helicity = Tw + Wr (*solid line*) for three magnetic field configurations at $y = z = 0$. The initial field and the final field are for run 2 and the Lundquist field has $\alpha R = 2.90$. Note that the final field has been shifted to the right by the displacement of the kink.

This expression is valid for a constant twist tube (i.e., for the initial state of most of our runs) but is only approximate for a general magnetic field profile. Nevertheless it gives us a way of estimating the behavior of twist as the tube evolves.

The initial field-line helicity for run 2, along with Wr and Tw, is plotted in the top panel of Figure 17. For comparison, the helicity for a number of field lines that intersect the $\hat{\psi}$-axis at the final equilibrium are plotted in the center panel of the same figure. While the helicity is no longer exactly its initial value, it is significantly closer to it than is that of the Lundquist solution. The helicity of the Lundquist field is shown in the next panel. At the center of the tube, the helicity is too low by a factor of 2.5, so the $m = 1$ part of the equilibrium must play a large role in bringing the helicity close to its initial value. At the edge of the tube, the helicity of the Lundquist field tends to infinity, which is a reason why the $m = 0$ equilibrium field does not match a Lundquist field profile near the outer edge of the tube. The other reason is that the outer edge of the tube needs magnetic
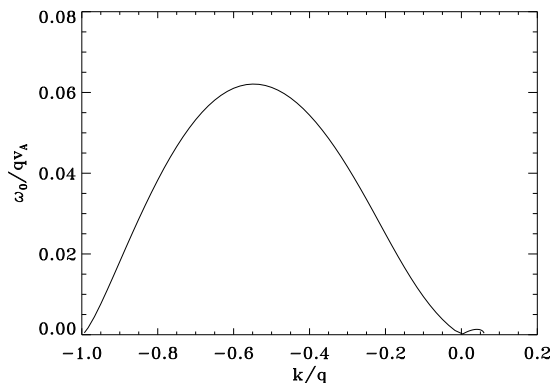

FIG. 18.—Predicted Gold-Hoyle dispersion relation (growth rate ω_0 as a function of wavenumber k) for a cutoff radius of $qR = 3\pi/2$. For a larger cutoff radius the curve is the same except near $k/q = 0$, where the growth rate is somewhat larger.

forces to counteract the excess external gas pressure. Note that as the calculation of twist is approximate. No significance should be attached to the exact values of helicity calculated; only the trends are meaningful.

We interpret these results to mean that the cylindrically symmetric part of a kink-unstable flux tube approaches a Lundquist field when the tube kinks. However, as the local helicity must be approximately conserved in these low-resistivity conditions, the tube is forced to take on an additional $m = 1$ component. This component, when added to the $m = 0$ component, gives each field line a helicity close to its initial helicity. The $m = 1$ Chandrasekhar-Kendall functions do not satisfy this helicity conservation condition, and the $m = 1$ component of the kink equilibrium fields are therefore quite different from the Chandrasekhar-Kendall functions. It is interesting that in this kinked equilibrium the balance between twist and writhe has been rearranged so that writhe contributes more to the helicity than it did initially, presumably because this is energetically favorable.

5.5. Gold-Hoyle Simulation

The initial equilibrium for the Gold-Hoyle simulation is

$$B_z = \frac{B_0}{1 + q^2 r^2}, \quad B_\theta = \frac{q r B_0}{1 + q^2 r^2}. \quad (31)$$

For this equilibrium flux tube q defines the only scale length. The field never goes to zero, so there is no clear choice of where the outer edge of the tube should be. We choose to make this outer edge lie at $r = R = \pi/2$, giving $B_z(R)/B_z(0) = 0.043$. Note that for this equilibrium, our simple instability criterion $q_{cr} = a^{1/2}$ predicts marginal stability. Upon numerical integration of the eigenfunction equation (see § 4 of LLF), however, we find an instability with a nonzero, though small, growth rate. Since q defines the tube uniquely, and also sets the size scale for the problem, the normalized growth rate ω_0/qv_A will be a function only of the normalized wavenumber k/q. This function is plotted in Figure 18. This figure shows a growth rate profile similar to that calculated for Gold-Hoyle tubes by Mikic, Schnack, & Van Hoven (1990) and by Craig, Robb, & Sneyd (1990). In the numerical simulation, the growth rate is a factor of 2 smaller than predicted (as seen in Fig. 6). The tube also takes an extraordinarily long time to saturate, compared to the other tubes: $\tau_{sat} \sim 30/\omega_0$ in contrast to the factor of 10 for the other tubes. In addition, the magnetic profile does not change much, the displacement is one of the smaller ones for any simulation (see Fig. 9), and α does not become much more uniform than it was initially.

6. DISCUSSION

It has been suggested by Tanaka (1991), Kurokawa et al. (1994), and Leka et al. (1996) that δ-spot active regions are formed by kinked flux tubes. We have pursued this suggestion by performing an investigation of highly twisted, kink-unstable flux tubes. Our objective is first to develop a clear understanding of how the nonlinear kink instability evolves, and second to see how well the kink mode evolution does in terms of explaining some properties of δ-spot regions. In the model, we propose that the flux tubes become unstable to the current driven kink instability during their rise through the convection zone. They then evolve into a kinked equilibrium and continue rising to the surface. Our linear study (LLF) indicates that as the tube expands upon rising

through the gravitationally stratified convection zone, it becomes more kink-unstable. This leads us to postulate that the apex of a rising flux tube will be the most likely location of a developing kink. Thus, as shown in Figure 1, most of the flux tube may still be in a simple Ω shape, while the apex has been deformed into a helical configuration. This helical apex, upon emerging into the photosphere and above, will create a bipolar magnetic region that behaves differently from those formed by an unkinked tube. The opposite-polarity regions will remain close to each other as the tube rises farther, and they will rotate about one another. In contrast, as a normal Ω-loop rises farther, the opposite polarities will separate from each other and will not rotate.

Our earlier study (LLF) was devoted to the investigation of the kink instability in the convection zone, i.e., in a high-β environment. That paper studied the linear instability of convection zone flux tubes, and found that those flux tubes could be unstable for a large range of magnetic profiles. In this paper, we modeled the nonlinear behavior of these kinking flux tubes. Our three-dimensional MHD code verified the results of our linear study, showing that tubes we expected to be unstable in fact did become unstable, and grew at the predicted growth rates and with the predicted velocity profiles. With this same code, we then explored the nonlinear evolution of the instability, allowing us to find saturation times and kinked equilibrium profiles. For the range of tubes studied (with the notable exception of the Gold-Hoyle tube), the saturation time was approximately 10 linear e-folding times, where this e-folding time is predicted by our linear theory. The final equilibrium of the kinked tube is characterized by a cylindrically symmetric constant-α, force-free field plus a nonconstant-α, force-free $m = 1$ field, which ensures that the local helicity is approximately preserved, since there is an absence of significant reconnection.

For the range of magnetic field profiles investigated, we found the kink amplitudes to be rather small, about 10%–40% of the tube radius. While not large enough to initiate reconnection, this does indicate that the tube geometry can be significantly distorted by the kink instability. Most important, the tubes reached a helical equilibrium, indicating that it is reasonable to expect tubes to emerge through the photosphere with kinked shapes. In other words, what we find suggests significant changes in tube orientation away from, e.g., Hale configurations, but we do not see 90° or 180° changes in orientation. We can say that kinks have the same sign of writhe as of twist, in contrast to what would occur if observed kinked tubes came about through external plasma motions.

In the future we will study kinking flux tubes in a more realistic convection zone environment by allowing them to expand as they evolve. This is meant to simulate the expansion a buoyant flux tube experiences as it rises into lower pressure regions of the convection zone. Our linear stability calculations indicate that the expansion of flux tubes can make them more kink-unstable. We therefore believe that studying the evolution of an initially kink-stable flux tube as it expands to an unstable state and then kinks will be an important part of our study. We also plan to study a flux tube as it evolves under the influence of multiple unstable modes (i.e., modes of different wavenumbers). The presence of multiple modes will be more realistic in that it would break the helical symmetry we have in the simulations reported on here, and it would potentially produce a tube with a localized kink, as shown in Figure 1.

REFERENCES

Antiochos, S., & Dahlburg, R. 1997, Sol. Phys., 174, 5
Anzer, U. 1968, Sol. Phys., 3, 298
Barnes, C., & Sturrock, P. 1972, ApJ, 174, 659
Baty, H. 1996, A&A, 308, 935
Berger, M., & Field, G. 1984, J. Fluid Mech., 147, 133
Bernstein, I. B., Frieman, E. A., Kruskal, M. D., & Kulsrud, R. M. 1958, Proc. R. Soc. London A, 244, 17
Caligari, P., Moreno-Insertis, F., & Schüssler, M. 1995, ApJ, 441, 886
Canuto, C., Hussaini, M., Quarteroni, A., & Zang, T. 1987, Spectral Methods in Fluid Mechanics (New York: Springer)
Chandrasekhar, S., & Kendall, P. 1957, ApJ, 126, 457
Choudhuri, A., & Gilman, P. 1987, ApJ, 316, 788
Courant, R., & Hilbert, D. 1989, Methods of Mathematical Physics, Vol. 1 (New York: Wiley)
Craig, I. J. D., Robb, T. D., & Sneyd, A. D. 1990, Ap&SS, 166, 289
Craig, I. J. D., & Sneyd, A. D. 1990, ApJ, 357, 653
Dahlburg, R., & Antiochos, S. 1997, Adv. Space Res., 19, 1781
Dahlburg, R., Antiochos, S., & Norton, D. 1997, Phys. Rev. E, 56, 2094
Dahlburg, R., & Norton, D. 1995, in Small Scale Structures in Three-dimensional Hydrodynamic and Magnetohydrodynamic Turbulence, ed. M. Meneguzzi, A. Pouquet, & P. Sulem (Heidelberg: Springer), 317
Dahlburg, R., & Picone, J. 1989, Phys. Fluids B, 1, 2153
DeLuca, E., & Gilman, P. 1991, in Solar Interior and Atmosphere, ed. A. N. Cox, W. C. Livingston, & M. S. Matthews (Tucson: Univ. Arizona Press), 275
Fan, Y., Fisher, G., & DeLuca, E. 1993, ApJ, 405, 390
Freidberg, J. P. 1987, Ideal Magnetohydrodynamics (New York: Plenum)
Goedbloed, J., & Hagebeuk, H. 1972, Phys. Fluids, 15, 1090
Gold, T., & Hoyle, F. 1960, MNRAS, 120, 89

Hood, A. W., & Priest, E. R. 1980, Sol. Phys., 66, 113
Hughes, D. W. 1992, in Sunspots, Theory and Observations, ed. J. H. Thomas & N. O. Weiss (Dordrecht: Kluwer), 371
Kruskal, M. D., Johnson, J. L., Gottlieb, M. D., & Goldman, L. M. 1958, Phys. Fluids, 1, 421
Kurokawa, H., Kitai, R., Kawai, G., Shibata, K., Yaji, K., Ichimoto, K., Nitta, N., & Zhang, H. 1994, in Proc. Kofu Symp, NRO Rep. 360, ed. S. Enome & T. Hirayama (Tucson: Univ. Arizona Press), 275
Leka, K., Canfield, R., McClymont, A., & van Driel Gesztelyi, L. 1996, ApJ, 462, 547
Linton, M. G., Longcope, D. W., & Fisher, G. H. 1996, ApJ, 469, 954 (LLF)
Lites, B. W., Low, B. C., Martinez Pillet, V., Seagraves, P., Skumanich, A., Frank, Z. A., Shine, R. A., & Tsuneta, S. 1995, ApJ, 446, 887
Longcope, D. W., & Fisher, G. H. 1998, ApJ, submitted
Longcope, D. W., & Klapper, I. 1997, ApJ, 488, 443
Lundquist, S. 1951, Phys. Rev., 83, 307
Mikic, Z., Schnack, D. D., & Van Hoven, G. 1990, ApJ, 361, 690
Moffatt, H., & Ricca, R. 1992, Proc. R. Soc. London A, 439, 411
Moreno-Insertis, F., Caligari, P., & Schüssler, M. 1994, Sol. Phys., 153, 449
Panton, R. L. 1996, Incompressible Flow (New York: Wiley)
Pevtsov, A. A., & Canfield, R. C. 1997, ApJ, submitted.
Roberts, P. H. 1956, ApJ, 124, 430
Shafranov, V. D. 1957, J. Nucl. Energy II, 5, 86
Tanaka, K. 1980, in Proc. Solar-Terrestrial Predictions, Vol. 3, ed. R. Donnelly, (NOAA-ERL)
———. 1991, Sol. Phys., 136, 133
Taylor, J. 1986, Rev. Mod. Phys., 58, 741
Zirin, H. 1988, Astrophysics of the Sun (Cambridge: Cambridge Univ. Press)